*J. Synchrotron Rad.* (1999). **6**, 964–972

# The soft X-ray spectroscopy beamline at the LNLS: technical description and commissioning results

**M. Abbate,* F. C. Vicentin, V. Compagnon-Cailhol, M. C. Rocha and H. Tolentino**

*Laboratório Nacional de Luz Síncrotron, CNPq, Caixa Postal 6192, 13083-970 Campinas SP, Brazil. E-mail: miguel@fisica.ufpr.br*

(*Received 29 September 1998; accepted 14 June 1999*)

The soft X-ray spectroscopy beamline installed at a bending-magnet source in the LNLS is presented. A technical description of the main elements is given and some selected commissioning results are shown. The beamline optics was designed to cover the soft X-ray energy range from 790 up to 4000 eV. The bending-magnet source has a critical energy of 2.08 keV and delivers $\sim10^{12}$ photons $s^{-1}$ $mradH^{-1}$ (0.1% bandwidth)$^{-1}$ (100 mA)$^{-1}$. The focusing element is a gold-coated toroidal mirror operating at an angle of incidence of 1°. The double-crystal monochromator has three pairs of crystals which can be selected by a lateral translation. The UHV experimental station is equipped with an ion gun, an electron gun, a LEED optics and an electron analyser. The beamline is intended for X-ray absorption, photoemission, reflectivity and dichroism experiments. The beamline has been installed, commissioned, and is now open to the external users community.

**Keywords: soft X-ray spectroscopy; beamline instrumentation.**

## 1. Introduction

The soft X-ray spectroscopy beamline installed at a bending-magnet source in the LNLS is presented. A technical description of the main elements is given and some selected commissioning results are shown. This material is intended to be used as a reference by external users and beamline managers.

There is an increasing interest in the use of synchrotron radiation sources. This interest is motivated by the excellent characteristics of this kind of radiation. For instance, the synchrotron light is some orders of magnitude more intense than conventional sources. The radiation is highly collimated, which is a great advantage in the design of the beamlines. The spectrum of the emitted light is continuous from the IR up to the X-ray range. The light emitted in the plane of the orbit is linearly polarized, but elliptically polarized light can be obtained above (or below) the orbit plane. The light is emitted in short pulses which can be used to study the dynamic response of a system. For these reasons, synchrotron radiation is very useful for studying the atomic, electronic and magnetic properties of materials (Winick & Doniach, 1980; Greaves & Munro, 1989; Kunz, 1979).

The LNLS synchrotron light source is based on a 1.37 GeV electron storage ring. The injection is accomplished at low energy using a 120 MeV linear accelerator. The storage ring is a third-generation light source with a critical energy of 2.08 keV. The circumference of the storage ring is 93.21 m and the mean radius is 14.83 m. The magnet lattice is a sixfold-symmetry double-bend Chasman-Green achromat design. The double-bend achromats are separated by six 2.95 m-long dispersion-free straight sections. Up to four of these sections can be used for insertion devices. The other two sections are occupied by the injection set-up and the RF cavity. The storage ring has already attained the design current of 100 mA at 1.37 GeV. The current lifetime has already reached the design value of 10 h at 100 mA.

**Table 1**
Technical characteristics of the crystals used in the monochromator.

| Crystal | 2*d* spacing (Å) | Energy range (eV) | Comment |
|---|---|---|---|
| Si(111) | 6.271 | 2010–11390 | High resolution |
| InSb(11$\underline{1}$) | 7.480 | 1680–9540 | High intensity |
| Beryl(10$\bar{1}$0) | 15.954 | 790–4475 | Low energy |

The LNLS is now operating with seven beamlines which are open to the external users community; four of them are dedicated to structural studies and the other three to spectroscopic techniques (Rodrigues *et al.*, 1998; Craievich & Rodrigues, 1997). The four beamlines devoted to structural studies are X-ray diffraction (XRD), X-ray absorption fine structure (XAFS), small-angle X-ray scattering (SAXS) and protein crystallography (PCr). The three beamlines dedicated to spectroscopic studies are toroidal-grating monochromator (TGM), spherical-grating monochromator (SGM) and soft X-ray spectroscopy (SXS). Three more beamlines are expected to begin their operation in 1998; these are X-ray fluorescence (XRF), X-ray instrumentation (XRI) and microfabrication (MF).

The soft X-ray absorption beamline was installed during the second semester of 1996, was commissioned during the first semester of 1997, and has been open to the external users community since July 1997. The beamline optics was designed to cover the soft X-ray energy range from 790 up to 4000 eV. The bending-magnet source has a critical energy of 2.08 keV and delivers $\sim 10^{12}$ photons $\mathrm{s}^{-1}$ $\mathrm{mradH}^{-1}$ (0.1% bandwidth)$^{-1}$ (100 mA)$^{-1}$. The focusing element is a gold-coated toroidal mirror operating at an angle of incidence of 1°. The double-crystal monochromator has three pairs of crystals which can be selected by a lateral translation. The UHV experimental station is equipped with an ion gun, an electron gun, a LEED optics and an electron analyser. The beamline is intended for X-ray absorption, photoemission, reflectivity and dichroism experiments. The beamline characteristics are similar to those of the JUMBO beamline at SSRL (Hussain *et al.*, 1982).

## 2. Beamline description

### 2.1. *General description*

The soft X-ray spectroscopy beamline is installed at a bending-magnet source in the storage ring. The layout of the main components of the soft X-ray spectroscopy beamline is shown in Fig. 1. These components are (*a*) the bending-magnet source, (*b*) the front-end section, (*c*) the focusing mirror, (*d*) the double-crystal monochromator and (*e*) the experimental station. There is also a set of slits and filters in front of the mirror chamber and a set of slits in front of the monochromator. The shield wall, located between the front end and the mirror chamber, is made out of concrete and has a thickness of 60 cm. All the critical components were designed, constructed and commissioned entirely at the LNLS.

### 2.2. *Vacuum overview*

The beamline is connected to the storage ring without any beryllium window to avoid unnecessary absorption. Therefore, the whole beamline has to be in a vacuum compatible with the storage ring. This means that the base pressure in the beamline has to be maintained in the low $10^{-9}$ mbar range. The vacuum is obtained using three ionic pumps located in the front-end section ($270\,\mathrm{l\,s^{-1}}$), the mirror chamber ($120\,\mathrm{l\,s^{-1}}$) and the monochromator ($400\,\mathrm{l\,s^{-1}}$). There are also two smaller ionic pumps ($120\,\mathrm{l\,s^{-1}}$) in the straight sections connecting the mirror to the monochromator and the monochromator to the experimental station. The experimental station is pumped with a turbomolecular pump and its base pressure is in the low $10^{-10}$ mbar range. The pressure is controlled using cold cathode gauges located in the front-end section, the mirror chamber, the monochromator and the experimental station. All the subsystems in the beamline are separated by gate valves and can be vented independently.

### 2.3. *Bending magnet*

The soft X-ray spectroscopy beamline is connected to the 4° exit port of the D04 bending magnet. The bending radius is 2.735 m and the bending field is 1.67 T for an electron energy of 1.37 GeV. The relativistic factor $\gamma$ is 2680, the critical wavelength is 5.95 Å and the critical energy is 2.08 keV. The horizontal and vertical dimensions (FWHM) of the source are 830 and 165 µm, respectively. The vertical divergence of the source at the critical energy, which is roughly given by $1/\gamma$, is 370 µrad.

The calculated photon flux produced by the bending-magnet source for a stored current of 100 mA at 1.37 GeV is shown in Fig. 2. The photon flux distribution presents a broad maximum in the soft X-ray energy region. The expected photon flux at the sample position should be of the order of $10^{12}$ photons $\mathrm{s}^{-1}$ $\mathrm{mradH}^{-1}$ (0.1% bandwidth)$^{-1}$ (100 mA)$^{-1}$. The measured photon flux will be smaller due to losses caused by absorption in the various optical elements (filter, mirror and monochromator).

One of the most interesting features of synchrotron radiation concerns the polarization of the light. The light emitted in the plane of the orbit is linearly polarized and away from this plane is elliptically polarized. In some studies, like in magnetic circular dichroism, it is necessary to have a large circular polarization. The linear and circular polarization rate are defined in terms of the Stokes parameters as $s_1/s_0$ and $s_3/s_0$, respectively (Born & Wolf, 1975). The circular polarization rate increases very rapidly with the offset angle. At the same time, however, the relative intensity decreases abruptly with this angle. We found in magnetic circular dichroism experiments that the optimum offset angle is ~0.52 mrad. At this angle the circular

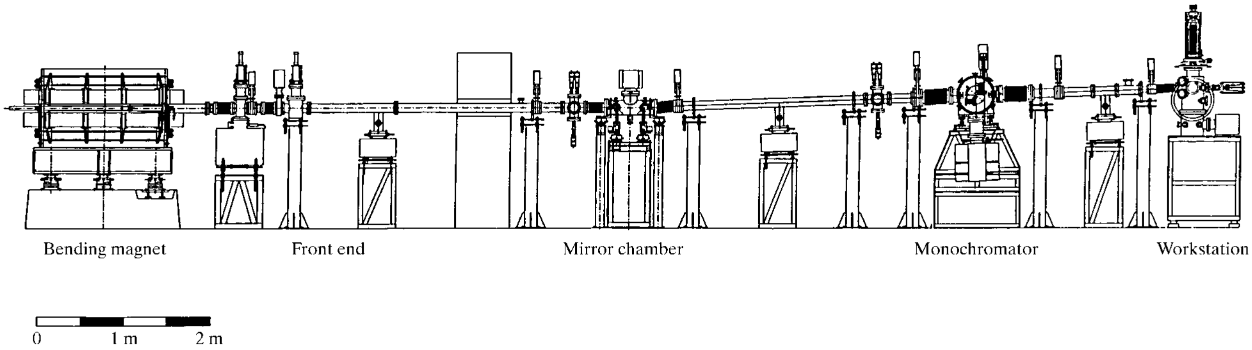

**Figure 1**
Layout of the main components in the soft X-ray spectroscopy beamline.

polarization rate is ~90% and the relative intensity is still 30%.

### 2.4. *Front-end section*

The front-end section is located between the bending-magnet source and the shield wall. This section contains several components which are devoted to radiation and vacuum safety. The main components are (*a*) a photon mask, (*b*) a photon shutter, (*c*) a gate valve, (*d*) a fast-closing valve, (*e*) a $\gamma$-ray shutter and (*f*) a fast vacuum sensor. The photon mask is made out of copper and is cooled by water; the horizontal acceptance angle defined by the mask is 12 mrad. The photon shutter is a copper block cooled by water and is mounted on a pneumatic actuator; this shutter is used to protect the other elements from radiation damage and heat load. The gate valve is used to isolate the vacuum of the storage ring from the rest of the beamline. The fast-closing valve was installed to prevent an accidental air inrush into the storage ring; this valve is interlocked to a fast vacuum sensor located in front of the mirror chamber. The $\gamma$-ray shutter is a thick lead block and is also mounted on a pneumatic actuator; this shutter is used to attenuate the $\gamma$-rays produced by bremsstrahlung during the injection.

### 2.5. *Slits and filters*

The first set of slits and filters is located in front of the mirror chamber; the distance of the slits from the bending-magnet source is 6 m. The slits are used to collimate the photon beam both in the horizontal and vertical directions. The jaws of the slits are made out of tantalum and the body of the slits out of copper. We choose tantalum for the jaws because it has a large absorption coefficient for hard X-rays. We choose copper for the body of the slits because it has a large thermal conductivity. The horizontal and vertical apertures of the slits are normally set to 60 and 1 mm, respectively; these apertures give a horizontal and vertical acceptance of 10 and 0.16 mrad, respectively. There is also a second set of collimating slits in front of the monochromator chamber.

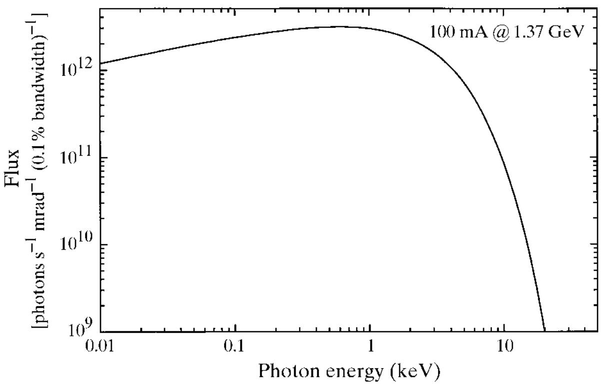

**Figure 2**
Photon flux produced by the bending magnet as a function of photon energy.

There can be up to three different absorption filters mounted on a sliding copper frame. These filters are mainly used to attenuate the IR–VIS–UV components of the spectrum; this low-energy radiation is barred to protect the beryl crystals in the monochromator. The main absorption filter used in the beamline is a commercial 1 µm carbon foil. The calculated transmission coefficient for this filter as a function of the photon energy is shown in the lower panel of Fig. 3. The calculation shows that the transmission in the soft X-ray energy range (from 1 to 4 keV) is very good. We observed that aluminium filters are not resistant enough to withstand the intense heat load generated by the radiation. In addition, the aluminium filters are also undesirable in the soft X-ray energy range because they absorb at the Al *K* edge.

### 2.6. *Focusing mirror*

The focusing element is a gold-coated toroidal mirror made out of zerodur and operating at an angle of incidence of 1°. We choose a toroidal shape because it gives a reasonably good focusing in both the horizontal and vertical directions. The substrate was made out of zerodur to ensure a good thermomechanical stability and it was covered by 400 Å of gold to enhance the X-ray reflectivity. The calculated reflectivity of gold as a function of the photon energy for an angle of incidence of 1° is plotted in the upper panel of Fig. 3. The resulting reflectivity is reasonably high up to 4000 eV and starts to decay at higher energies. The absorption of high-energy photons is desirable because it reduces the heat load on the crystals, and

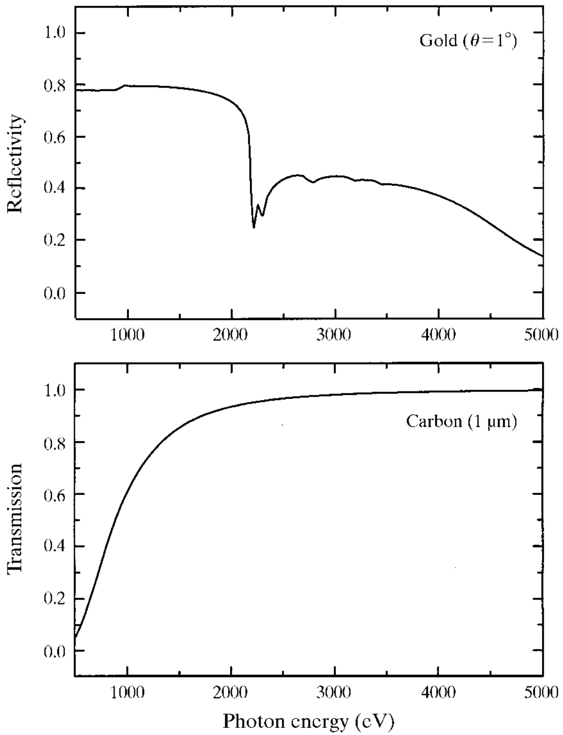

**Figure 3**
Mirror reflectivity (top) and foil transmission (bottom) as a function of the photon energy.

also because it suppresses the high-energy harmonic contamination.

The mirror is located at 6.5 m from the bending-magnet source, halfway between the source and the experimental station. The source–mirror to mirror–sample distance ratio was chosen equal to 1:1 to minimize the comma aberration. This ratio results in a magnification of 1, thus mapping the photon source onto the sample position. The main deviations from this mapping are caused by the slope error of the mirror surface. Additional deviations are due to aberrations caused by the toroidal shape of the reflecting surface. The measured spot size at the sample position is approximately 2 × 3 mm$^2$. These values are in good agreement with the predicted FWHM (1.5 × 3 mm$^2$) of a *SHADOW* simulation (Welnak *et al.*, 1992).

### 2.7. *Monochromator*

The UHV double-crystal monochromator has three pairs of crystals which can be selected by a lateral translation. This is a great advantage because there is no need to open the chamber to exchange crystals. The three pairs of crystals installed in the monochromator at the moment are Si(111), InSb(111) and beryl(10$\bar{1}$0). The rotation of the goniometer is achieved by a translation stage connected to a drum by a thin steel wire. The step of the translation stage is 0.5 µm and the diameter of the drum is 200 mm; this results in an angular resolution of 5 µrad per step. This angular resolution is good enough for most applications in soft X-ray spectroscopy. The useful angular range of the goniometer, because of limitations in the crystal dimensions, is from 10 to 80°.

A description of the double-crystal monochromator and details on the elastic translators design can be found elsewhere (Correa *et al.*, 1992; Tolentino *et al.*, 1995). Briefly, the double-crystal monochromator operates in the constant offset mode and always illuminates the same region of the crystals. In order to achieve this, the position of the crystals is controlled with two perpendicular elastic translators. These elastic translators were chosen because they ensure the repeatability of the positioning to the required accuracy. The fine adjustment of the crystals is performed by a solenoid acting on a magnet mounted on a weak link arm; the accuracy of this set-up allows adjustment of the parallelism of the crystal to better than 0.1 arcsec. This set-up can be used to reject higher-energy harmonic contamination by detuning and also to measure the rocking curves of the crystals.

Table 1 gives the 2*d* spacing of the three crystals as well as the photon energy range defined by the useful angular range. The lowest energy, 790 eV, is obtained using the beryl(10$\bar{1}$0) crystals at an angle of incidence of 80°. The highest energy, 11390 eV, is obtained using Si(111) at an angle of incidence of 10°. However, the reflectivity of the focusing mirror limits the useful energy range of the beamline to ~4000 eV. Table 1 also gives the main characteristic of each crystal: Si(111) has the best intrinsic

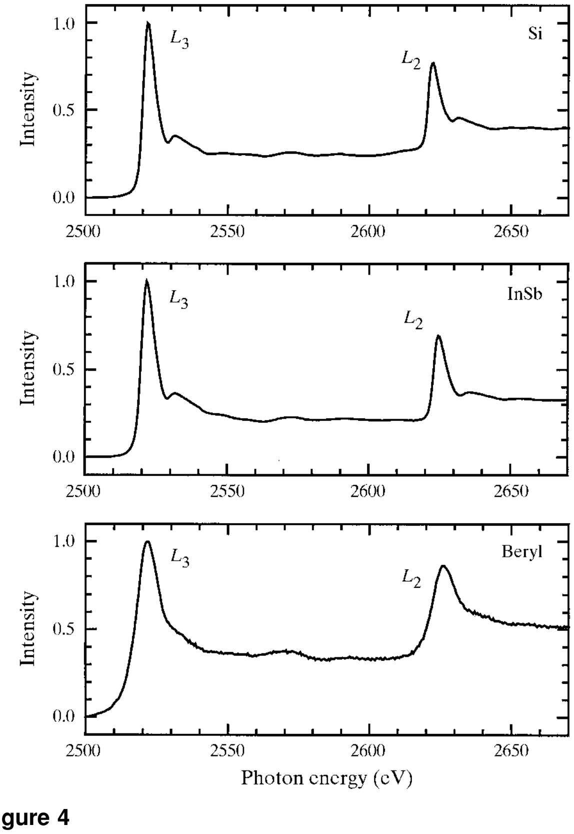

**Figure 4**
Mo $L_{2,3}$ X-ray absorption edges taken with the three different crystal pairs.

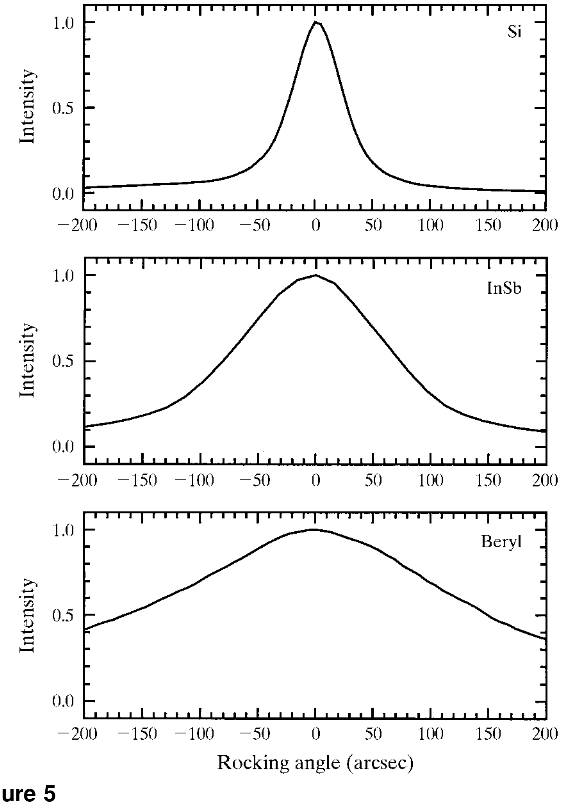

**Figure 5**
Rocking curves of Si(111), InSb(111) and beryl(10$\bar{1}$0) taken at 2500 eV.

resolution and is good for high-resolution studies; InSb(111) has the largest reflectivity and is good for high-intensity studies; beryl(10$\bar{1}$0) has the largest $2d$ spacing and is good for low-energy studies. These characteristics are confirmed by comparing the performance of the three crystals at 2500 eV (see below).

The double-crystal monochromator has a negative influence on circularly polarized light. This component is very strongly suppressed by the monochromator for Bragg angles close to 45° (Brewster angle). This is due to the cancellation of the component polarized in the scattering plane for this particular angle (circularly polarized light is a linear combination of light polarized parallel and perpendicular to the scattering plane; if one of these components is cancelled the circular polarization is completely suppressed). The circular polarization rate for the beryl crystals is very small for energies close to 1100 eV; this energy range corresponds to a Bragg angle of close to 45° (Brewster angle) for these crystals.

### 2.8. *Experimental station*

The UHV chamber of the experimental station has a modular design with three different levels. The lower level is dedicated to the vacuum components; this level has a turbomolecular pump, a cold cathode gauge and a pre-vacuum valve. The intermediate level is devoted to sample preparation; this level has up to three evaporators, and a low-energy ion gun for sputtering. The upper level is dedicated to the characterization of the samples; this level has an electron analyser, a LEED optics, an electron gun and a twin-anode X-ray source. The set-up is completed with a high-precision $XYZ$–$\theta$ manipulator sitting on top of the experimental station. The experimental station can be either coupled to the soft X-ray spectroscopy beamline or can be used as an stand-alone spectroscopy system.

The high-precision manipulator has five feedthroughs which can be used for electrical and thermocouple connections. The temperature of the sample can be controlled in the 80–600 K range using a liquid nitrogen cryostat and a halogen lamp. Even higher temperatures can be obtained flashing the sample with a high-energy electron beam. The temperature of the samples can be estimated using a thermocouple attached to the sample holder. The surface of the samples can be cleaned using either low-energy argon sputtering or by scraping with a diamond file. Ferromagnetic samples can be magnetized for dichroism experiments using a 10 A pulsed horseshoe electromagnet. Gases can be admitted into the UHV chamber for adsorption studies using a controlled leak valve. Monolayers or multilayers can be grown *in situ* using up to three different Knudsen cell evaporators.

The soft X-ray absorption spectroscopy experimental station is intended for photoemission, X-ray absorption, reflectivity and dichroism experiments. The photoemission experiments can be carried out using a hemispherical electrostatic electron energy analyser. The X-ray absorption spectra are usually measured in the total electron yield mode using an open channeltron. However, partial or Auger electron yield measurements can be implemented using the electron energy analyser. The reflectivity of the samples can be measured at grazing incidence angles using a photodiode array located in the forward direction. Linear dichroism effects can be investigated using linearly polarized light from the orbit plane. Circular dichroism experi-

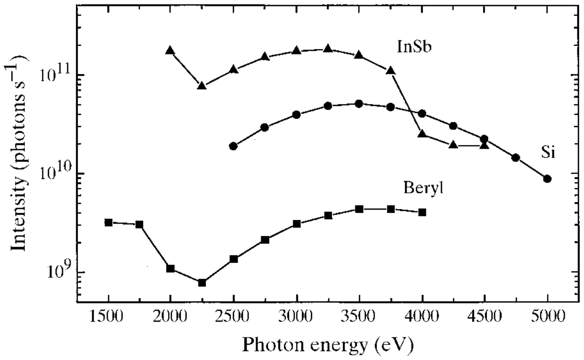

**Figure 6**
Photon flux measured at the sample position as a function of the photon energy.

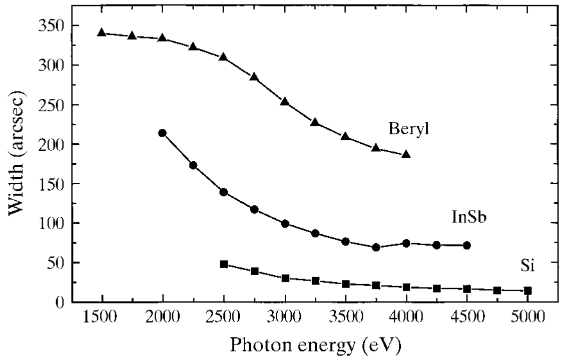

**Figure 7**
Rocking width of the three different crystal pairs as a function of the photon energy.

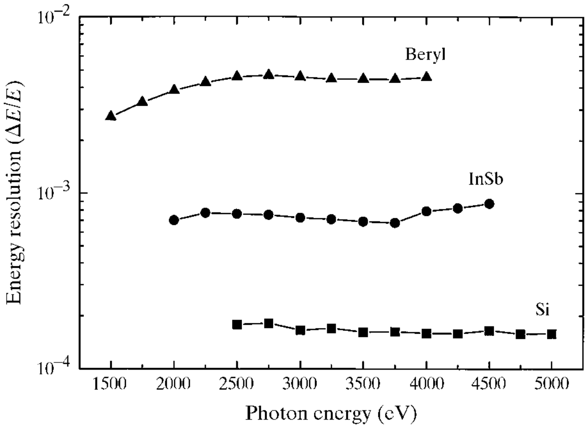

**Figure 8**
Intrinsic energy resolution of the crystals as a function of the photon energy.

ments can be performed using circularly polarized light from above (or below) the orbit plane.

## 3. Commissioning results

### 3.1. *Mo $L_{2,3}$ X-ray absorption*

Fig. 4 shows the Mo $L_{2,3}$ X-ray absorption edges taken with the three different crystal pairs. The spectra were taken in the total electron yield mode collecting the emitted current with an open channeltron. The energy scale was calibrated using the known value of the Mo $L_3$ X-ray absorption edge (2520 eV). The spectra provide useful information on the relative performance of the three different crystal pairs. The Mo $L_{2,3}$ X-ray absorption edges are ideally suited for a comparison because they present rather sharp features. The spectra present two strong peaks, attributed to the $L_3$ and $L_2$ edges, followed by the corresponding XANES structure. The $L_3$ and $L_2$ edges are assigned, respectively, to transitions from the Mo $2p_{3/2}$ and $2p_{1/2}$ levels into unoccupied $4d$ states. The spectra taken with the Si(111) and InSb(111) crystals are quite similar; they exhibit a good energy resolution and an excellent signal-to-noise ratio. The spectrum taken with the beryl($10\bar{1}0$) crystals shows a poorer statistic and worse energy resolution; these drawbacks are related to the relatively low reflectivity and wide rocking curve of these crystals.

### 3.2. *Rocking curves at 2500 eV*

Fig. 5 shows the rocking curves of the Si(111), InSb(111) and beryl($10\bar{1}0$) crystals taken at 2500 eV. The diffracted intensity was recorded using a commercial photodiode with a 100% quantum efficiency. The offset angle scale was calibrated previously measuring the deflection of an He–Ne laser beam. The full width at half maximum of the rocking curves increases from Si(111) to InSb(111) and beryl($10\bar{1}0$). The intrinsic resolution of the crystals is closely related to the corresponding width of the rocking curve. The energy resolution decreases in the sequence from Si(111) to InSb(111) and beryl($10\bar{1}0$). These values confirm that the Si(111) crystals are the best suited for high-energy resolution studies. The unusually wide rocking curve of beryl($10\bar{1}0$) is ascribed to the mosaicity of the crystals. The photon flux at 2500 eV was estimated using the known calibration of the photodiode. The photon intensity decreases in the sequence from InSb(111) to Si(111) and beryl($10\bar{1}0$). This confirms that the InSb(111) crystals are the best suited for high-intensity studies.

### 3.3. *Throughput of the monochromator*

Fig. 6 shows the photon flux at the sample position for the different crystals as a function of the photon energy. The photon intensity was measured using a calibrated photodiode with a 100% quantum efficiency. The parallelism of the crystals was readjusted for each energy position taking a rocking curve. The overall reflectivity of the crystals decreases in the sequence from InSb(111) to Si(111) and beryl($10\bar{1}0$). The reflectivity of the InSb(111) crystals for a given energy is significantly larger than for Si(111) and beryl($10\bar{1}0$). This can be understood taking into account that the X-ray reflectivity tends to increase for the heavier elements. The intensity should drop at higher energies following the spectral distribution of the source; this is somewhat compensated by a larger reflectivity at higher energies (smaller Bragg angles). The dip around 2250 eV in beryl($10\bar{1}0$) and InSb(111) is attributed to

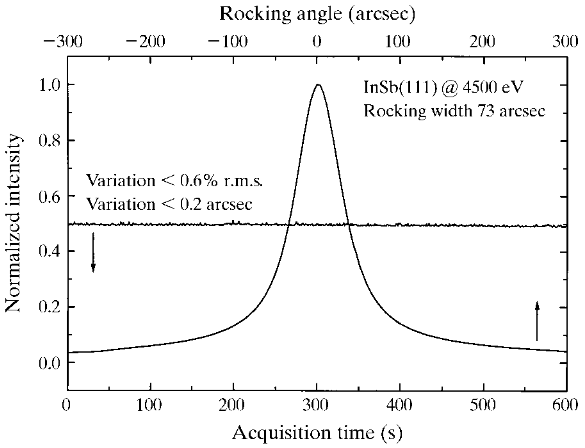

**Figure 9**
Stability of the monochromator as a function of time measured at the flank of the rocking curve of InSb(111).

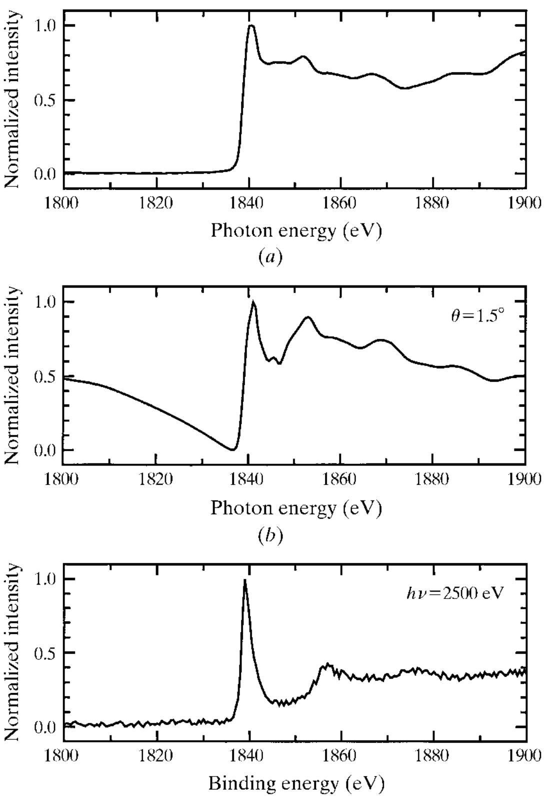

**Figure 10**
Si 1*s* X-ray spectra: (*a*) absorption, (*b*) reflectivity and (*c*) photoemission.

Au $M_{4,5}$ absorption in the mirror coating. The drop above 3500 eV in the InSb(111) curve is assigned to In $L_{2,3}$ and Sb $L_{2,3}$ self-absorption in the crystals. The spectra taken in these energy regions have to be normalized to take into account these variations.

### 3.4. *Rocking width versus energy*

Fig. 7 shows the width of the rocking curve for the different crystals as a function of the photon energy. The photon intensity was measured using a calibrated photodiode with a 100% quantum efficiency. The vertical slits in front of the mirror were set to 1 mm giving a vertical divergence of ~34 arcsec. The width of the rocking curve increases along the sequence from Si(111) to InSb(111) and beryl(10$\bar{1}$0). The differences in the rocking curves can be understood taking into account the different crystal qualities. The Si(111) and InSb(111) crystals are high-quality (dislocation-free) single crystals. The abnormally large width of the rocking curve for beryl(10$\bar{1}$0) is attributed to the mosaicity of the crystals. The rocking widths of Si(111) and InSb(111) show the expected decay at higher energies. The unusual functional dependence for beryl(10$\bar{1}$0) is again attributed to crystal mosaicity; this effect is larger at higher energies because the light illuminates a larger part of the crystals. The small bump in the data of InSb(111) around 4000–4500 eV is related to self-absorption at the In $L_{2,3}$ and Sb $L_{2,3}$ edges. The width of the corresponding rocking curve determines the intrinsic energy resolution of a given crystal pair. The intrinsic energy resolution can be estimated using the differential form of Bragg's law: $\Delta E/E = -\cot\theta_B\,\Delta\theta$, where $\theta_B$ is the corresponding Bragg angle and $\Delta\theta$ is the width of the rocking curve. The intrinsic energy resolution estimated using this equation is shown in Fig. 8; the best energy resolution in this case corresponds to the Si(111) crystals, as expected.

### 3.5. *Stability of the monochromator*

Fig. 9 shows the photon intensity delivered by the monochromator at the sample position as a function of time. The monochromator was operating with the InSb(111) crystals and the photon energy was set to 4500 eV. The photon intensity was measured using a calibrated photodiode with a 100% quantum efficiency. The InSb(111) crystals were adjusted at the flank of the rocking curve to enhance the sensitivity. The photon intensity was recorded during 600 s, which is the typical time needed to record an X-ray spectrum. The noise in the photon intensity gives a measure of the mechanical instabilities in the monochromator. The variation of the photon intensity for this particularly sensitive situation was less than 0.6% r.m.s. (a much smaller variation would be obtained for the crystals adjusted at the top of the rocking curve). The overall angular stability of the pairs of crystals in these operating conditions was better than 0.2 arcsec; this value was estimated from the variation of the photon intensity and the

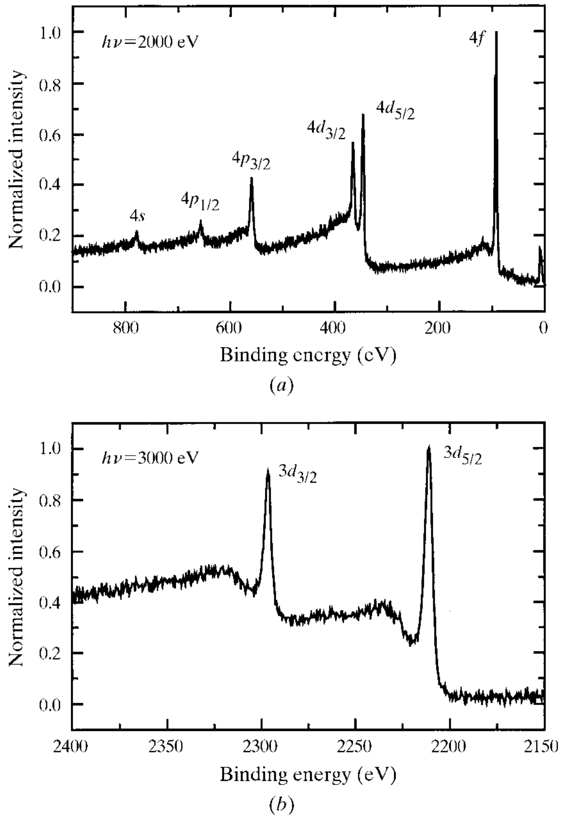

(*a*)

(*b*)

**Figure 11**

Au X-ray photoemission spectra: (*a*) 4*s*–4*f* core levels, and (*b*) 3*d* core levels.

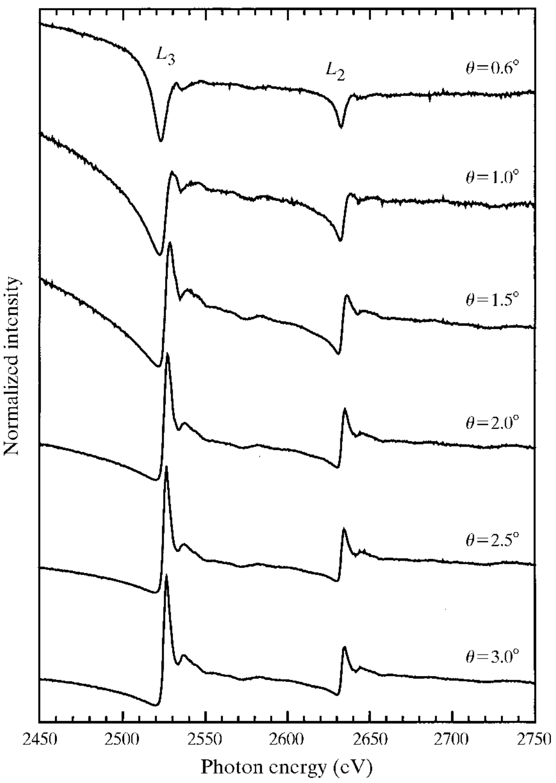

**Figure 12**

Mo $L_{2,3}$ X-ray reflectivity spectra taken at different angles of incidence.

slope of the rocking curve at the flank. The angular stability of the monochromator is sufficient for most applications in soft X-ray spectroscopy.

### 3.6. *Case study: Si 1s X-ray spectra*

Fig. 10 shows three different Si 1*s* X-ray spectra including (*a*) absorption, (*b*) reflectivity and (*c*) photoemission. These spectra illustrate the main experimental techniques available at the soft X-ray spectroscopy beamline. The Si *K* X-ray absorption spectrum was taken in the total electron yield mode collecting the emitted current with an open channeltron. The sample was a 25 × 30 × 3 mm slab cut from an Si single crystal oriented along the (111) direction. The monochromator was operating with the InSb(111) crystals and the vertical slits were set to 1 mm. The energy scale was calibrated setting the edge of the absorption spectrum to the Si 1*s* binding energy of 1839 eV. The energy step was set to 1 eV and the time per step was set to 1 s. The spectrum corresponds to transitions from the Si 1*s* level into unoccupied Si 3*p* states in the conduction band. The spectrum presents a strong absorption peak followed by the usual XANES structure at higher energies; the XANES structure is in good agreement with previous results obtained at the JUMBO beamline (Hussain *et al.*, 1982).

The Si *K* X-ray reflectivity spectrum was taken with a calibrated photodiode mounted on a sliding arm in the forward direction. The angle of incidence was set to 1.5° which is larger than the estimated critical angle for Si at this energy (~0.9°). The X-ray reflectivity spectrum is closely related to the complex refractive index of the material. The complex refractive index presents considerable resonant structure close to an absorption edge. Above the critical angle the spectrum is dominated by the imaginary part of the refractive index. The imaginary part of the refractive index is directly related to the absorption coefficient; this helps to explain the close similarities between the absorption and reflectivity spectra. The main effect caused by the real part of the refractive index at this angle of incidence is the dip observed in the pre-edge region.

The Si 1*s* X-ray photoemission spectrum was taken using the electrostatic electron energy analyser. The monochromator was operating with the InSb(111) crystals and the photon energy was set to 2500 eV. The analyser was operated in the constant pass energy mode and the pass energy was set to 46.93 eV; the energy resolution of the analyser at this pass energy is approximately 0.7 eV. The usual sense of the binding energy scale was inverted for a more straightforward comparison. The main peak in the photoemission spectrum is attributed to quasi-elastic transitions from the Si 1*s* core level. The strong bump located 18 eV above the main peak is assigned to the plasmon loss satellite; this satellite is similar to those observed in the standard Si 2*s* and 2*p* photoemission spectra (Chastain, 1992).

### 3.7. *Au X-ray photoemission*

Fig. 11 shows the Au X-ray photoemission spectra of (*a*) the 4*s*–4*f* and (*b*) the 3*d* core levels. The monochromator was operating with the InSb(111) crystals and the photon energy was set to 2000 and 3000 eV, respectively. The pass energy of the analyser was set to 46.93 eV giving an energy resolution of approximately 0.7 eV; the overall energy resolution estimated from the Fermi edge of the sample was better than 1 eV. The energy scale was calibrated using the known energy of the core levels and the Fermi level of the sample. The Au 4*s*–4*f* spectrum shows several peaks which are attributed to transitions from the 4*s*–4*f* core levels; the spectrum is in very good agreement with the spectrum obtained using conventional X-ray sources (Chastain, 1992). The photoemission facility at this beamline is not characterized by a high intensity or a high energy resolution. Higher intensity could be obtained at the TGM beamline and higher energy resolution at the SGM beamline. The main advantage of the soft X-ray spectroscopy beamline in a photoemission experiment is the extended energy range. This is illustrated in the photoemission spectrum of the Au 3*d* inner core levels; these levels could not be studied using the other beamlines or the standard X-ray anodes.

### 3.8. *Mo $L_{2,3}$ X-ray reflectivity*

Fig. 12 shows the Mo $L_{2,3}$ X-ray reflectivity spectra taken at different angles of incidence. The monochromator was operating with the InSb(111) crystals and the vertical slits

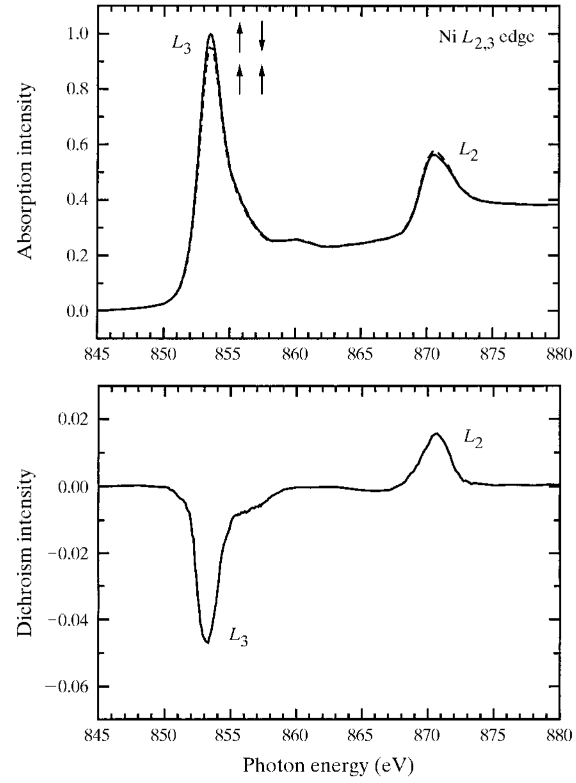

**Figure 13**
Magnetic circular dichroism at the Ni $L_{2,3}$ X-ray absorption edges.

were set to 1 mm. The energy scale was calibrated setting the Mo $L_3$ edge of the X-ray absorption spectrum to 2520 eV. The X-ray reflectivity spectrum was taken with a calibrated photodiode mounted on a sliding arm in the forward direction. The critical angle of incidence for Mo in this photon energy range is approximately 1.5°. The X-ray reflectivity spectrum is closely related to the complex refractive index of the material; the refractive index presents considerable resonant structure close to the absorption edges. Above the critical angle, the spectrum is dominated by the imaginary part of the refractive index. In this regime the X-ray reflectivity spectrum resembles very closely the X-ray absorption spectrum. This kind of behaviour is observed in the reflectivity spectra for angles of incidence above 1.5°. Below the critical angle the reflectivity spectrum is dictated by the real part of the refractive index. In this case the reflectivity spectrum presents a strong dip close to the absorption edges. This kind of behaviour is observed in the reflectivity spectra taken at 0.6° and, to a lesser extent, 1.0°. The spectrum taken at the critical angle, 1.5°, reflects both influences and presents a mixed character.

### 3.9. *Ni $L_{2,3}$ magnetic circular dichroism*

Fig. 13 shows the magnetic circular dichroism effect in the Ni $L_{2,3}$ X-ray absorption edges. The monochromator was operating with the beryl($10\bar{1}0$) crystals and the slits were set 0.52 mrad below the orbit plane. The effective circular polarization rate after the monochromator in this energy range is ~50% (Lefebvre *et al.*, 1994). The sample was a thin disc (diameter 10 mm, height 2 mm) cut from an Ni single crystal oriented along the (111) direction. The sample was magnetized at room temperature using an NdFeB permanent magnet. The X-ray absorption spectra were taken in the total electron yield mode measuring the emitted current with an electrometer. The spectra present two strong absorption peaks which are attributed to the Ni $L_3$ and $L_2$ X-ray absorption edges. These peaks correspond to transitions from the Ni $2p_{3/2}$ and $2p_{1/2}$ levels into unoccupied Ni $3d$ states. The spectra taken with the magnetization parallel and antiparallel to the helicity of the photons are different. The difference is the magnetic circular dichroism signal corresponding to the X-ray absorption spectra; the spectrum is in very good agreement with previous results obtained at the DRAGON beamline (Chen *et al.*, 1990). The dichroism intensity obtained at the DRAGON beamline is almost two times higher, mainly because the grazing-incidence optics of the DRAGON better preserves the helicity of the photons.

## 4. Summary and conclusions

The soft X-ray spectroscopy beamline installed at a bending-magnet source in the LNLS was presented. A technical description of the main elements was given and some selected commissioning results were shown. The beamline optics was designed to cover the soft X-ray energy range from 790 up to 4000 eV. The bending-magnet source has a critical energy of 2.08 keV and delivers $\sim 10^{12}$ photons $s^{-1}$ mradH$^{-1}$ (0.1% bandwidth)$^{-1}$ (100 mA)$^{-1}$. The focusing element is a gold-coated toroidal mirror operating at an angle of incidence of 1°. The double-crystal monochromator has three pairs of crystals which can be selected by a lateral translation. The UHV experimental station is equipped with an ion gun, an electron gun, a LEED optics and an electron analyser. The beamline is intended for X-ray absorption, photoemission, reflectivity and dichroism experiments. The beamline has been installed, commissioned, and is now open to the external users community.

We would like to thank the technical staff of LNLS, especially A. C. Mattiazo, for skilful assistance. This work was partially supported by Conselho Nacional de Desenvolvimento Científico e Tecnológico (CNPq), Fundação de Amparo à Pesquisa do Estado de São Paulo (FAPESP), and Programa de Apoio a Nucleos de Excelência (PRONEX).

## References

Born, M. & Wolf, E. (1975). *Principles of Optics.* Oxford: Pergamon Press.

Chastain, J. (1992). *Handbook of Photoelectron Spectroscopy.* Eden Praire: Perkin-Elmer.

Chen, C. T., Sette, F., Ma, Y. J. & Modesti, S. (1990). *Phys. Rev. B*, **42**, 7262.

Correa, M. C., Tolentino, H., Craievich, A. F. & Cusatis, C. (1992). *Rev. Sci. Instrum.* **63**, 896–898.

Craievich, A. F. & Rodrigues, A. R. D. (1997). *Braz. J. Phys.* **27**, 417–424.

Greaves, G. N. & Munro, I. H. (1989). *Synchrotron Radiation: Sources and Applications.* Bristol: IOP Publishing.

Hussain, Z., Umbach, E., Shirley, D. A., Stöhr, J. & Feldhaus, J. (1982). *Nucl. Instrum. Methods*, **195**, 115–131.

Kunz, C. (1979). *Synchrotron Radiation: Techniques and Applications.* Berlin: Springer-Verlag.

Lefebvre, D., Sainctavit, Ph. & Malgrange, C. (1994). *Rev. Sci. Instrum.* **65**, 2556–2561.

Rodrigues, A. R. D., Craievich, A. F. & Gonçalves da Silva, C. E. T. (1998). *J. Synchrotron Rad.***5**, 1157–1161.

Tolentino, H., Durr, J., Mazzaro, I., Udron, D. & Cusatis, C. (1995). *Rev. Sci. Instrum.* **66**, 1806–1808.

Welnak, C., Anderson, P., Khan, M., Singh, S. & Cerrina, F. (1992). *Rev. Sci. Instrum.* **63**, 865–868.

Winick, H. & Doniach, S. (1980). *Synchrotron Radiation Research.* New York: Plenum.